Acta Materialia 262 (2024) 119421

Contents lists available at ScienceDirect

Acta Materialia

journal homepage: www.elsevier.com/locate/actamat

Full length article

Revealing hot tear formation dynamics in Al–Cu alloys with X-ray radiography

Insung Han [a,*], Shikang Feng [a], Fabian Wilde [b], Patrick S. Grant [a], Enzo Liotti [a,*]

[a] Department of Materials, University of Oxford, Oxford OX1 3PH, United Kingdom
[b] Institute of Materials Research, Helmholtz-Zentrum Hereon, Max–Planck-Straße 1, 21502 Geesthacht, Germany

ARTICLE INFO

Keywords:
Hot tears
Solidification
Al alloys
Synchrotron X-ray radiography
Interdendritic flow

ABSTRACT

Hot tears can arise during the late part of alloy solidification because of the shrinkage of isolated liquid as it turns to solid and may have a catastrophic effect on cast tensile properties. Although there are correlations to suggest alloy hot tear sensitivity to casting conditions, they do not capture the influence of microstructure on tearing, such as second-phase particles or intermetallic compounds (IMCs) commonly present in engineering alloys. We use *in situ* X-ray radiography to quantify the formation and growth behaviour of hot tears in Al-5Cu and Al-5Cu-1Fe alloys during solidification. An automated hot tear detection, tracking and merging algorithm is developed and applied to reveal the role of Fe-rich IMC particles, typical of recycled alloys, on hot tear behaviour. These defects are termed hot tears here on the basis of their complex, extended inter-connected morphology, distinct from more rounded shrinkage porosity. We also visualise and quantify the velocity of interdendritic flow driven by solidification shrinkage, and estimate the pressure changes due to shrinkage. Hot tearing starts at lower solid fraction when IMCs are present due to reduced interdendritic flow, and hot tear formation is more spatially homogeneous, less clustered and more numerous. We show that the largest, most damaging hot tears form from many merging events, that is enhanced by the presence of IMCs.

1. Introduction

Hot tears are severe structural defects that may develop during the casting of engineering alloys towards the end of solidification due to the shrinkage (up to 5 vol. %) of the liquid as it turns to solid. Because the rate of heat extraction inevitably varies from place to place in a casting, especially with changes in section thickness, the local rate of shrinkage during solidification also varies spatially. The liquid alloy flows from regions of zero or low shrinkage to regions of high shrinkage, over distances that may approach the dimensions of the casting. As solidification proceeds, the solid fraction increases and the permeability of the solid/liquid mixture (the mushy zone) decreases, and the shrinkage driven flow becomes more difficult. Eventually, the flow – or "feeding" of shrinkage – in some regions of the casting becomes impossible and the ongoing shrinkage of this now isolated liquid progressively decreases the local liquid pressure. At a critical negative pressure, the residual liquid (1%–10%), typically distributed along grain boundaries, fails mechanically, often called decoherence, and an extended planar, convoluted tear is formed. Differences between shrinkage porosity and hot tear defects are made either by the local pressure or stress state: negative hydrostatic pressure for porosity and a uniaxial tensile stress for hot tears; or morphology based on rounded shrinkage pores or elongated planar cracks and tears. Here we use the term hot tear throughout on the basis of defect morphology shown subsequently, but note their formation is related principally to pressure drop in the liquid.

When a large hot tear forms, there may also be significant and sudden movement of an extended region of the mushy grain network, causing the flow of either solute-rich or solute-denuded liquid into the tear to form local segregates. Hot tearing is exacerbated by the presence of pre-existing gas bubbles in the liquid and stress-raising geometric features that promote tensile stress such as corners which might fracture in shaped castings.

Note that hot tears form only when liquid is still present, and any planar defect formation in the solid state by thermal contraction is more normally termed hot cracking.

Hot tears are defects of millimetre or greater scale that undermine tensile mechanical properties such as yield strength, fatigue life, ductility and toughness, and are generally considered catastrophic defects. In shaped castings, hot tears cannot usually be healed since geometric complexity precludes thermomechanical processing such as forging, although in limited cases welding can be used to heal surface-breaking tears. Even in simple billet or slab shaped wrought alloy

* Corresponding authors.
E-mail addresses: insung.han@materials.ox.ac.uk (I. Han), enzo.liotti@materials.ox.ac.uk (E. Liotti).

https://doi.org/10.1016/j.actamat.2023.119421
Received 15 May 2023; Received in revised form 2 October 2023; Accepted 8 October 2023
Available online 10 October 2023

castings designed for subsequent rolling, forging or other procedure, the undermining effects of hot tears and segregates usually cannot be ameliorated.

Because of the technological importance of avoiding tears, considerable effort has been spent in understanding and describing the phenomenon, using a mixture of theory, simulation and experiment [1–24]. The best known approach was introduced by Campbell [1] and the concept of a cracking susceptibility coefficient (CSC) [18] was then defined, the magnitude of which indicates the tendency of an alloy to form a hot tear:

$$CSC = \frac{\alpha \Delta T L \lambda}{l^2} \cdot \frac{t_V}{t_R} \quad (1)$$

where α is the thermal expansion coefficient, ΔT is the temperature interval between when the first solid appears and the last liquid disappears, L relates to the size of the casting, λ is the grain size, l relates to the size of the region of the cast that cannot be fed (typically the last-to-freeze, isolated liquid), t_V is the time period during which cracks can propagate between grains, and t_R is the time period over which any stress-relaxation processes are able to operate [1]. Qualitatively, the CSC captures the experimentally observed influence of practical parameters, and for example, explains why near eutectic composition alloys (such as cast irons and Al–Si alloys) with a small or no freezing range (i.e. $\Delta T \approx 0$) have low hot tearing tendency and hence are widely used in the casting industry [19,25]. Other parameters in the CSC, such as the time periods for hot tearing and stress relaxation, or the size of the "hot spot" that contains the last to freeze liquid, can be challenging to assess in practice. The CSC also has no ability to describe local pressure or stress state effects on tear or pore formation.

Nonetheless, using this type of correlation, hot tearing has been introduced into casting simulations that incorporate other key phenomena such as fluid flow, and are used to optimise casting design [4–6, 26]. Alongside post-solidification metallographic investigation, *in situ* observations of hot tearing have been used to calibrate or validate these simulations, with generally good agreement between simulation and theory albeit with some fitting of parameters [8–13]. Initially, *in situ* observation of hot tears involved transparent organic alloys such as succinonitrile (SCN)-acetone, a metallic alloy analogue, which allowed real-time optical imaging of microstructural and defect evolution close to room temperature [27–29]. External forces have also been imposed on evolving microstructures to quantify some aspects of hot tear formation and growth under controlled conditions [8].

More recently, synchrotron X-rays have been used for *in situ* imaging of hot tearing in metallurgical alloys directly [9–13,20]. For example, X-ray computed tomography (XCT) was conducted on a solidifying alloy under tensile deformation that captured the formation and growth of hot tears in 3D [12,30]. XCT has also been combined with detailed simulations to evaluate the influence of secondary intermetallic compounds (IMCs) on liquid flow and the tendency for shrinkage-induced defect formation in Al alloys [13]. The influence of secondary IMCs on hot tearing, such as Al–Fe based IMCs in Al alloys that arise due to accumulated Fe from recycling [31,32], cannot be captured easily in expressions of the type in Eq. (1) [14,15]. On the other hand, while direct imaging studies have suggested influence of IMCs and other microstructural features on hot tearing, images have had insufficient temporal and/or spatial resolution to track the large number of hot tears required to ensure a representative description [8,11].

In this paper we present a methodology to capture the moment of hot tear formation, subsequent growth, and hot tear merging in aluminium alloys using fast (up to 100 Hz) synchrotron-based X-ray radiography. To understand the critical interdendritic liquid flow, up to the moment of hot tear formation, we also add a trace amount of Pb (~0.7 wt%) to the alloy to form fine X-ray absorbing Pb droplets that are tracked, frame to frame [20]. High resolution radiographs are processed through a hot tear detection and tracking algorithm based on advanced computer vision techniques. We apply the methodology to Al–Cu alloys, without and with Fe that forms secondary IMC particles, under different solidification conditions. Our principal objective is to understand the influence of Fe containing IMCs on hot tearing in Al alloys. We show significant spatial and temporal differences in hot tearing between the alloys. The differences relate principally to the direct effect of IMCs on the flow and sub-division of interdendritic liquid. Although IMCs lead to the early onset of hot tearing, they also homogenise hot tear spatial distribution, even in cases where the total area fraction of tears is increased. The largest hot tears arise from multiple hot tear propagation and merging events.

2. Methods

2.1. Sample preparation

Alloys of composition Al-5Cu and Al-5Cu-1Fe (all in wt.% and hereafter) were prepared from Al (99.999% purity), Al-80Cu master alloy and Al-75Fe master alloy. A trace amount of Pb (0.7%, 99.999% purity) was also added to form a fine dispersion of micron-sized Pb droplets in the liquid via a monotectic reaction. The micron-sized droplets were sufficiently small to be swept or "seeded" in the interdendritic flow during solidification, and were used to visualise and estimate liquid flow velocities in the final stages of solidification as described in [20]. Both alloys were also inoculated with 0.1% of Al-5Ti-B grain refiner to ensure an equiaxed, dendritic structure of the primary α-Al. The alloys were mixed at 750 °C in an induction furnace under Ar atmosphere. The melt was held for 10 min for homogenisation and then cast into a water-cooled Cu mould. The ingots were sectioned, ground and polished into 10 mm (width) × 20 mm (height) × 0.2 mm (thickness) sections for synchrotron radiography experiments.

2.2. Synchrotron X-ray radiography

Synchrotron X-ray radiography experiments were carried out at the DESY PETRA III synchrotron (Hamburg, Germany) at the P05 beamline operated by Helmholtz-Zentrum Hereon [33]. Samples were encapsulated between 100 μm thick BN sheets and mounted in our bespoke Bridgman furnace [34] under Ar atmosphere. Samples were heated and held at 690 °C for 5 min to homogenise the melt, and then cooled at rates of 0.5, 1, 2 and 4 °C s^{-1} to 510 °C, while acquiring images at 12.5, 25, 50 and 100 Hz respectively, to maintain one frame for every 0.04 °C change of temperature. The beamline was used in monochromatic mode with energy peaking at 19 keV. Two detectors with a different spatial resolution and field of view (FOV) were used: a Ximea CB500MG detector (spatial resolution: 1.1 μm, FOV: 4.51 × 3.38 mm^2) and KIT CMOS detector (spatial resolution: 1.284 μm, FOV: 6.55 × 4.92 mm^2). The detectors were coupled optically to a 200 μm LuAG:Ce scintillator screen with a five-fold magnification objective lens. Based on experience over a wide range of operating conditions, we estimated a temperature gradient of < 3 °C mm^{-1} across the FOV.

2.3. Hot tear analysis

2.3.1. Detection and tracking

The number of hot tears across the FOV in one experiment was usually too large to be robustly identified and tracked simultaneously by manual methods. Therefore, an automated procedure was developed. The hot tear detection algorithm was based on the pixel intensity difference obtained by subtracting two consecutive radiographic images [11], which were first flat-field corrected using a radiograph of the sample fully liquid (i.e. prior to the appearance of primary α-Al) using a MATLAB R2022a code. The resulting radiographic images were then segmented with an appropriate threshold to remove noise and an additional size/morphology-based filter was applied to suppress any remaining anomalies [35].

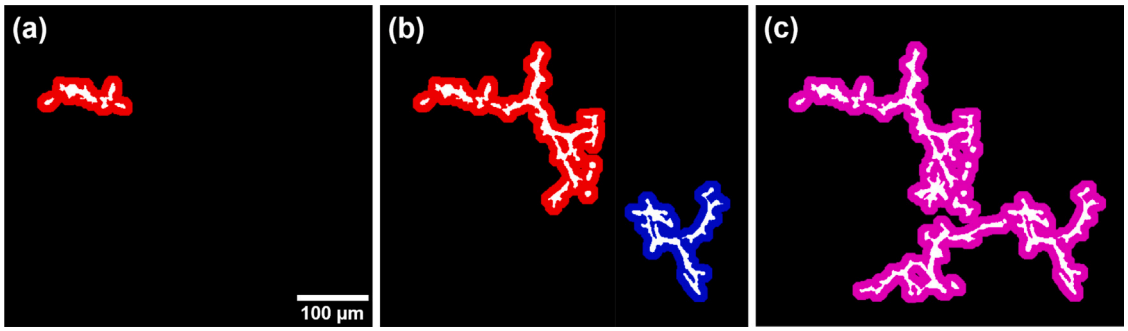

Fig. 1. Segmented hot tears (white) with their unique identifiers UIs (colours) according to the hot tear detection algorithm. White regions encapsulated by the same colour are considered a single hot tear. (a) Formation of a single hot tear at the early stage. (b) Growth of the hot tear in (a) and the formation of a new hot tear. (c) A merged hot tear from the two hot tears in (b). (For interpretation of the references to colour in this figure legend, the reader is referred to the web version of this article.)

An example of a hot tear detected using this approach, just after formation, is shown by the white pixels in Fig. 1(a). Very narrow hot tears sometimes appeared fragmented into several closely spaced pieces due to blurring. Therefore, to check if these fragments were separate hot tears or not, hot tear images were dilated slightly using a 10-pixel × 10-pixel kernel that assessed if fragments belonged to the same hot tear. An example of dilation is shown by the red pixels in Fig. 1(a). Once identified, a unique identifier (UI) was assigned to the tear and any solid or liquid phase outside the tear (black pixels in Fig. 1(a)) was ignored. Note that dilation was used only for identification purposes and all measurements, such as area fraction, were performed on non-dilated images. Once a tear was detected, it was assumed to be always present and only a change (e.g. growth) of the tear was recorded, i.e. detection was required only once per tear.

Fig. 1(b) is a subsequent frame showing the growth of the hot tear in Fig. 1(a) and the formation of a second tear nearby (in blue), which was assigned a different UI. In a later frame, shown in Fig. 1(c), the tears grew and merged and the merged tear was assigned a new UI and a new colour. Thus, the algorithm recorded three tear characteristics: nucleation, growth, and any merging. Subsequently, the data was processed off-line to give information on every tear formation position, associated time and temperature, its size and shape evolution, and any merging behaviour.

2.3.2. Shape factor

Fig. 1 suggests that useful information might arise if the shape of the hot tear could be conveniently described, since more extended planar tears are known to be the most damaging. As described in the Supplementary Information, a shape factor S_f was defined and used to record the shape of every tear. Fig. S1 shows that for $S_f \sim 1$, the hot tear is approximately equiaxed while $S_f \geq 1$ indicates a progressively more elongated hot tear.

2.3.3. Spatial distribution

The spatial distribution of hot tears was also quantified in terms of a clustering parameter R following the methodology given in [36], which is a measure of the variation in the distance between an object and its neighbours and is described in the Supplementary Information. The distances used in the analysis were those between the centroid of each hot tear at its earliest stage. As shown in Fig. S2 in the Supplementary Information, for $R = 1$, the distance to neighbours is random and the objects are randomly distributed; for $R < 1$, the objects are increasingly clustered while for $R > 1$, the objects are increasingly uniformly distributed as a regular grid or array.

2.3.4. Estimation of solid fraction

Because the onset of hot tearing is known to relate to a critical alloy solid fraction, the variation of solid fraction (f_s) with temperature for both alloys was calculated using FactSage v8.2 and the FTlite (FACT Light Metal Alloy) database [37] as shown in Fig. 2. So-called "Scheil" conditions, i.e. interfacial equilibrium but no far field equilibrium in the solid, were assumed. The trace of Pb was included in the simulation, but had no resolvable effect on the phase selection and the intermetallic formation temperature as Pb had no appreciable solid solubility in the IMCs and remained in the liquid to well below the eutectic temperature. Individual solidification paths of Al-5Cu and Al-5Cu-1Fe with and without Pb are shown in Fig. S3 in the Supplementary Information. Both alloys were calculated to have a liquid fraction of approximately 0.12 at the eutectic temperature (T_E = 547.9 °C). To estimate the solid fraction above f_s = 0.88, the solid fraction f_S was assumed to simply increase linearly from the frame at which f_s = 0.88 to the frame at which f_s = 1 determined manually from the radiographs. According to the solid fraction calculations in Fig. 2, the addition of Fe altered the solidification sequence, lowering the formation temperature of primary α-Al and leading to the formation of IMCs such as $Al_{13}Fe_4$, Al_6(Cu,Fe) and Al_7Cu_2Fe. In practice, our prior work on this alloy at the cooling rates used here has shown that $Al_{13}Fe_4$ and Al_6(Fe,Cu), which have limited solubility of Cu, do not form readily in Cu-rich liquid Al and instead stoichiometric Al_7Cu_2Fe, that bears a higher concentration of Cu, is obtained at higher undercoolings [38].

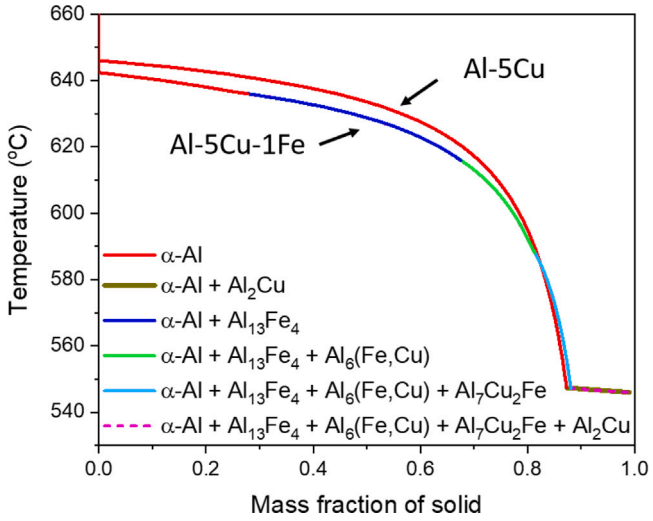

Fig. 2. Scheil solidification simulation for Al-5Cu and Al-5Cu-1Fe (with trace amount of Pb). Different colours represent different solid phase combinations during solidification. (For interpretation of the references to colour in this figure legend, the reader is referred to the web version of this article.)

Table 1
Summary of the experimental conditions and the number of repeats of each condition, and the number of sequences in which hot tears formed, given in parentheses.

Alloy composition	Cooling rate (°C s^{-1})			
	0.5	1.0	2.0	4.0
Al-5Cu	4 (1)	4 (3)	2 (2)	3 (0)
Al-5Cu-1Fe	5 (5)	6 (6)	3 (3)	3 (0)

2.3.5. Flow analysis

To confirm and visualise the liquid feeding due to solidification shrinkage, and to gain a sense of the scale and speed of liquid movement, interdendritic fluid flow was recorded by tracking the movement of the thousands of Pb droplets that formed as a micron-scale emulsion in the liquid, between the α-Al grains. The analysis of the droplet-liquid interaction, described in detail in [20], showed that the presence of the Pb droplets had minimal effect on the liquid flow. Direct observation confirmed that liquid flowed readily over distances many times the α-Al grain size in these pseudo-2D, thin samples.

From the measured droplet velocity distribution obtained by frame-to-frame tracking, it was possible to estimate the evolution of liquid velocities v_l in the interdendritic channels through a simple drag law, as described in detail in [20]:

$$\boldsymbol{v}_l = \boldsymbol{v}_d + \frac{r_d^2(\rho_d \frac{d\boldsymbol{v}_d}{dt} - \Delta\rho\boldsymbol{g})}{6\eta_l \frac{2\eta_l+3\eta_d}{\eta_l+\eta_d}} \quad (2)$$

where v_d is the velocity of the Pb droplets, r_d is their radius, ρ_d is the density of liquid Pb, $\Delta\rho = \rho_d - \rho_l$ is the density difference between the liquid in the interdendritic region and in the Pb droplets, $\boldsymbol{g}$ is the gravitational acceleration vector, η_l and η_d are the dynamic viscosity of the Al-5Cu-1Fe liquid and of the liquid in the droplet (99.82% Pb) respectively. The values of the parameters used for the calculation are given in Table S1, and more details on the assumptions, application and validity of Eq. (2) are given in [20].

3. Results and discussion

3.1. Radiograph sequences

In total we investigated 30 solidification sequences, 13 for Al-5Cu and 17 for Al-5Cu-1Fe, at four cooling rates of 0.5, 1, 2 and 4 °C s^{-1}. Hot tears occurred in 20 sequences, and only at cooling rates at or below 2 °C s^{-1}, as summarised in Table 1.

It may be surmised that at the highest cooling rate of 4 °C s^{-1} the time period during which resolvable tears could form (or nucleate), t_V in Eq. (1), was comparatively short and thus CSC was relatively small [21]. Fast cooling also led to a reduction in mean grain sizes, which were more able to accommodate solidification shrinkage [22]. For example, in the case of Al-5Cu, the mean grain size decreased from 246 ± 18 μm at 5 °C s^{-1} to 154± 6 μm at 4 °C s^{-1} (see Fig. S4 for more details).

Fig. 3 shows typical radiographs taken from solidification sequences of Al-5Cu and Al-5Cu-1Fe cooled at 1.0 °C s^{-1}. At $f_s = 0.5$ (Fig. 3(a,b)), the microstructure mainly comprised equiaxed α-Al grains surrounded by Cu-enriched liquid with Pb droplets in the interdendritic channels. Although not easily resolvable, note that in Al-5Cu-1Fe and consistent with the calculation in Fig. 2, IMCs were already present. In Fig. 3(c,d), the solid fraction increased to 0.8 and thousands of Pb droplets, 2 to 8 μm in diameter, were now clearly visible within the interdendritic channels. In the fully solid state, shown in Fig. 3(e,f), Al-5Cu had a slightly coarser microstructure with an average grain size of 201 ± 23 μm compared with 177 ± 21 μm of Al-5Cu-1Fe. The tears (highlighted in purple) appeared larger and more heterogeneously distributed in Al-5Cu. For example, the largest hot tear in Al-5Cu was 6.3×10^4 μm^2, approximately eight times larger than in Al-5Cu-1Fe.

The Al-5Cu microstructure in the late stages of solidification at 2 °C s^{-1} is shown in Fig. 4. The full field of view image at 546.5 °C and $f_s \sim 1$ (Fig. 4(a)) is similar to Al-5Cu in Fig. 3 but Fig. 4(b-d) show in detail the formation of hot tears in the region highlighted by the red box. Supplementary video 1 shows an example of the evolution of a hot tear. Hot tears started to appear at 548.3 °C, $f_s \sim 0.882$ and propagated quickly, within 1 s ($\Delta T < 2$ °C), and up to the beginning of the formation of the α-Al/Al_2Cu eutectic.

Similarly, Fig. 5 shows the formation of hot tears in the presence of IMCs in Al-5Cu-1Fe cooled at 0.5 °C s^{-1}. Hot tear formation began earlier, at a solid fraction as low as $f_s = 0.83$, and new hot tears continued to form over a large temperature range of up to 40 °C, until the final α-Al/Al_7Cu_2Fe/Al_2Cu eutectic reaction was complete. In Fig. 5(b–g), several plate-like IMCs are coincident with growing hot tears.

3.2. Interdendritic flow

Fig. 6 shows the evolution of the median interdendritic liquid velocities as a function of solid fraction. A total of 19 video sequences of Al-5Cu and Al-5Cu-1Fe cooled between 1 and 4 °C s^{-1} were analysed and data for each condition was obtained by combining data from at least two experiments. For Al-5Cu-1Fe, flow measurement up to a solid fraction of 0.88 was possible, capturing the initial stage of hot tear formation and before the eutectic reaction. For Al-5Cu, however, droplet movement was only detectable with acceptable accuracy up to a solid fraction of 0.81, so the interaction between the flow and hot tears could not be resolved. Nonetheless, readers are referred to the supplementary video 2 that gives a clearer impression of the extent and significant distance over which interdendritic flow took place, confirming the strong influence of solidification shrinkage even in these relatively thin samples. Note that many of the floating grains "flickered" in the videos because they were temporarily oriented as to satisfy Bragg conditions, diffracting a fraction of the X-rays and so appearing temporarily darker. This phenomenon has been observed in previous experiments when using a monochromatic beam, but it is more pronounced here because of the fast acquisition rate, which increased the probability of capturing a moving grain momentarily at a diffraction orientation. Instantaneous interdendritic liquid velocities ranged between 43 μm s^{-1} and 181 μm s^{-1} and were consistently higher in Al-5Cu, with a maximum difference of ~ 100 μm s^{-1} when comparing alloys at the same cooling rate and solid fraction. The overall median velocity was between 115 μm s^{-1} and 139 μm s^{-1} in Al-5Cu, and 85 μm s^{-1} and 100 μm s^{-1} in Al-5Cu-1Fe. Qualitatively, the flow appeared more uniform in Al-5Cu-1Fe, while in Al-5Cu there was more variability, such as the peak velocity changes between a solid fraction of 0.75 and 0.80 at 4 °C s^{-1}. There was no significant velocity dependency with cooling rate. Similar flow behaviour and median velocities between 114 and 152 μm s^{-1} were reported for an Al-1Pb alloy with equiaxed microstructure solidified under similar conditions [20].

The slower velocities in Al-5Cu-1Fe here might be ascribed to the presence of the IMCs in the interdendritic channels. In an investigation of the influence of IMCs on the interdendritic flow during the solidification of Al–Si–Cu alloys, which combined time-resolved tomography with flow simulation, IMCs had a constraining effect on the flow and reduced the liquid permeability of the mushy zone [13]. A modified Blake–Kozeny model for columnar microstructure permeability with a correction factor was proposed to relate this permeability loss to the IMC fraction (f_i), given as $(1 - \beta f_i)K$, where $\beta = 10$ or 15 for flow normal and parallel to the primary dendrite arms, and K is the Blake–Kozeny permeability [13]. Although the current work concerns equiaxed microstructures, for which the Kozeny–Carman model might be more appropriate [20], following [13] and assuming a maximum IMCs fraction of ~0.03 from the thermodynamics calculations gives a reduction in liquid permeability up to 45%, consistent with the lower measured velocities in Al-5Cu-1Fe.

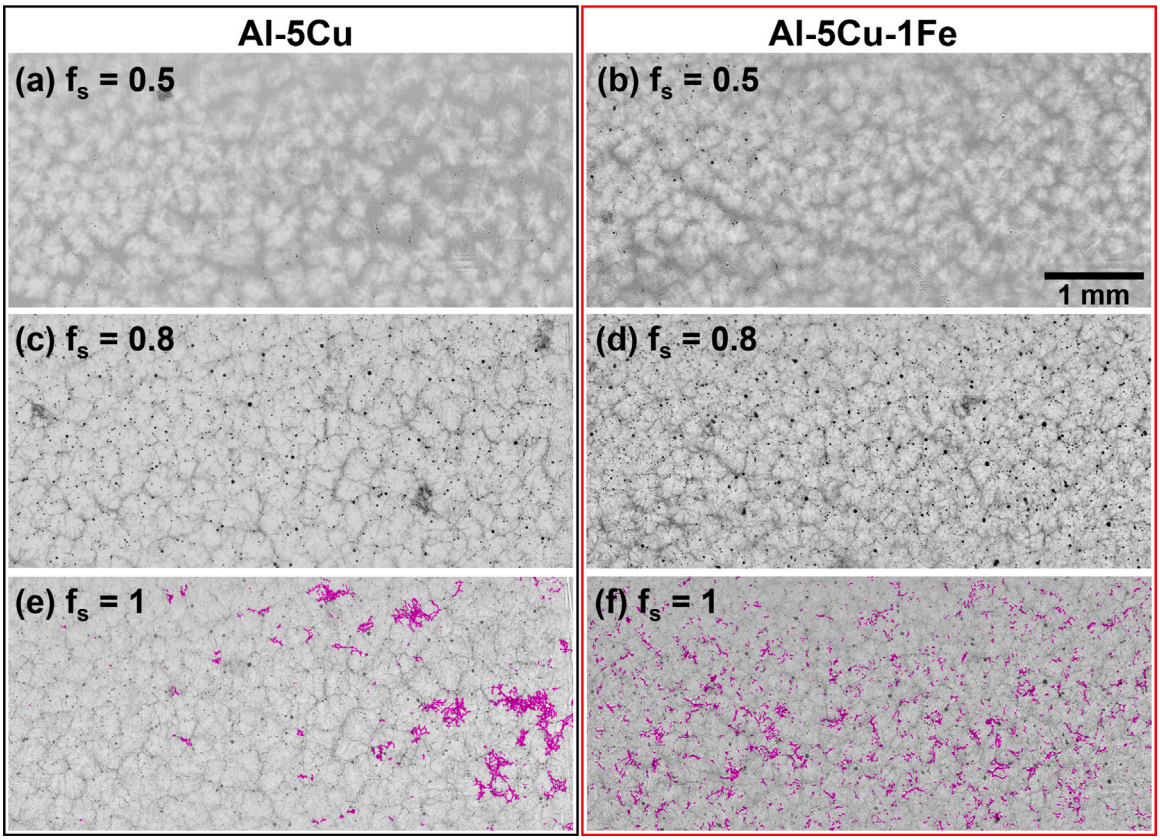

Fig. 3. Radiographs of the solidification of Al-5Cu (left column) and Al-5Cu-1Fe (right column) cooled at 1.0 °C s^{-1} showing the microstructure at a solid fraction of (a,b) 0.5, (c,d) 0.8, and (e,f) 1. Hot tears are highlighted in purple. Pb droplets (black) that flowed in the interdendritic regions are also visible. (For interpretation of the references to colour in this figure legend, the reader is referred to the web version of this article.)

3.3. Hot tear development

The evolution of the hot tear density as a function of solid fraction, grouped by alloy composition and cooling rate, is shown in Fig. 7.

Although the hot tear nucleation dynamics were qualitatively different, the critical solid fraction for hot tear formation was similar, close to $f_s = 0.88$. In all conditions the hot tear density was significantly higher in Al-5Cu-1Fe for which, on average, the final hot tear density was 49 ± 6 mm^{-2}, which was 5.5 times larger than for Al-5Cu. The hot tear density did not vary systematically with cooling rate.

In Al-5Cu, hot tear nucleation occurred either as a single burst just before or as the eutectic started to form at $f_s = 0.88$, and/or then semi-continuously when $f_s > 0.96$. The peak hot tear nucleation rate (see Fig. S5) was $\dot{n} \sim 7000$ (where $\dot{n}$ is defined as hot tear number per % solid per mm^2), whereas at $f_s > 0.96$, $\dot{n} < 500$. In Al-5Cu-1Fe, nucleation behaviour was more disperse, starting at a solid fraction as low as 0.83 with a rate of $\dot{n} \sim 1800$ and then increasing until the beginning of the eutectic formation at $f_s = 0.90$ and $\dot{n} \sim 6500$. The rate then decreased to $\dot{n} \sim 100$ before increasing briefly to $\dot{n} \sim 2000$ when $f_s > 0.95$. Increasing the cooling rate shifted the hot tear nucleation burst to slightly higher solid fractions, possibly because faster cooling delayed the formation of IMCs [38]. The critical solid fractions for hot tear formation are in very good agreement with reports for Al and Mg alloys [30,39–42].

The evolution of the total hot tear area (measured as the area fraction of hot tears in the field of view) followed similar trends to the hot tear density, as shown in Fig. 8. However, the difference between alloys was less pronounced. In Al-5Cu-1Fe, faster cooling led to a significant decrease in the hot tear area fraction from an average of 0.041 to 0.037 and 0.014, at 0.5, 1 and 2 °C s^{-1} respectively. There was no similar trend for Al-5Cu where the hot tear area was between 0.010 and 0.019 (note that there was more limited data available for Al-5Cu). Comparing hot tear area fraction in Fig. 8 with hot tear density in Fig. 7 suggests that hot tears were generally larger in Al-5Cu (Fig. S6). The data also show that the number of hot tears was significantly higher in Al-5Cu-1Fe, but growth of individual hot tears was reduced.

The higher hot tear nucleation in the Fe containing alloy is due to two main effects related to the presence of the IMCs between grains: (i) the increased physical segmentation of the interdendritic liquid into small, isolated pockets; and (ii) a larger pressure drop because of the reduced permeability of the liquid. Support for the segmentation of the liquid into isolated pockets by IMCs is provided by plotting the hot tear spatial distribution R against the hot tear density, as shown in Fig. 9.

Two clusters corresponding to the alloys are obtained, showing that in Al-5Cu hot tear nucleation both was lower and near randomly distributed ($\overline{R} = 1.03 \pm 0.18$), whereas in Al-5Cu-1Fe, there was more hot tear nucleation and hot tears were more regularly distributed ($\overline{R} = 1.15 \pm 0.04$).

Support for reduced permeability when IMCs are present uses the data in Fig. 6(a–b) for the liquid velocity v_l in Al-5Cu-1Fe to obtain the pressure drop ΔP in the liquid from Darcy's law [20]:

$$\Delta P = -v_l \frac{\eta_l}{(1 - f_i\beta)K} \tag{3}$$

where η_l is the dynamic viscosity of the Al-5Cu-1Fe liquid, K is the permeability of the liquid, f_i is the IMC fraction and β a correction factor. Assuming a Kozeny–Carman model for permeability for an equiaxed microstructure:

$$\Delta P = -v_l \frac{\eta_l}{(1 - f_i\beta)} \frac{180 f_s^2}{\lambda^2 (1 - f_s)^3} \tag{4}$$

where λ is the dendrite secondary arm spacing. In Al-5Cu-1Fe, the average critical solid fraction at 1 and 2 °C s^{-1} was $\overline{f_s}$ =0.86 and λ = 50 μm (as estimated from the radiographs). Assuming a flow parallel

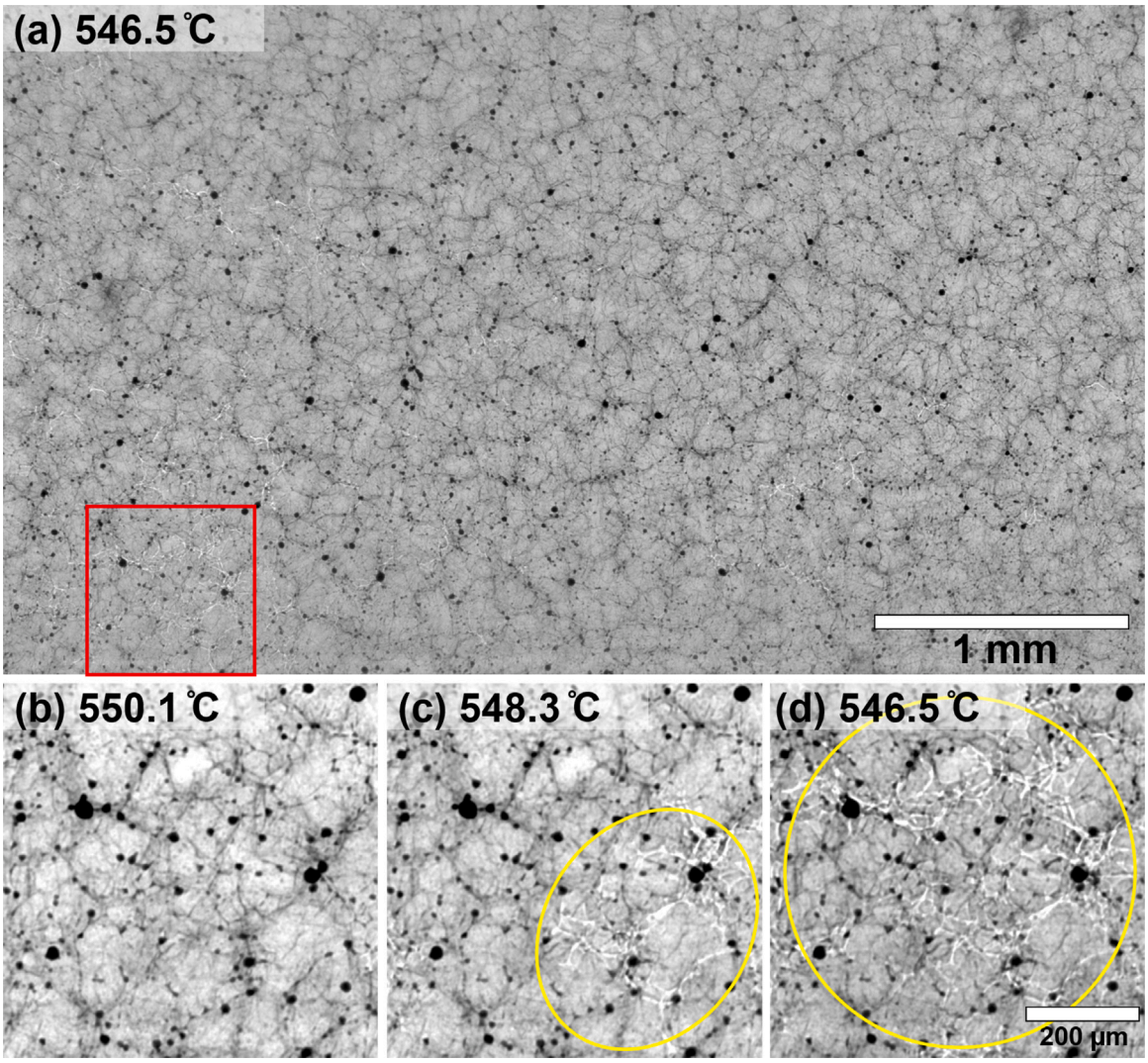

Fig. 4. Radiographic images of Al-5Cu cooled at 2 °C s^{-1}. (a) At 546.5 °C just below the eutectic point when $f_s \sim 1$. (b) Magnified view of the region highlighted by the red box in (a) at 550.1 °C ($f_s \sim 0.881$) showing equiaxed α-Al dendrites. (c,d) Hot tear formation and growth at 548.3 °C ($f_s \sim 0.882$) and 546.5 °C ($f_s \sim 1$), respectively. The areas with hot tears are highlighted with yellow circles. Note that the image contrast in (b–d) has been adjusted to better visualise the hot tears. (For interpretation of the references to colour in this figure legend, the reader is referred to the web version of this article.)

to the dendritic arms gives $\beta = 15$, and considering Eq. (4) gives the critical pressure change for hot tear formation as −3.5 to −4 MPa for $f_i = 0.03$, almost double that when IMCs are absent and $f_i = 0$.

The hot tear shape factor S_f at the end of solidification was calculated for 8508 individual hot tears and fitted to a log-normal distribution as shown in Fig. 10(a–c) for cooling rates of 0.5, 1 and 2 °C s^{-1}. The distributions were generally similar, but with some weak correlation with alloy composition and cooling rate. For Al-5Cu the median increased from 1.387 ± 0.215 to 1.427 ± 0.266 and 1.464 ± 0.263 at cooling rates of 0.5, 1 and 2 °C s^{-1} respectively. There was a similar but weaker trend in Al-5Cu-Fe, with the median increasing from 1.456 ± 0.61 to 1.466 ± 0.259 and 1.472 ± 0.269. Overall, despite the aforementioned small differences, there was weak hot tear growth direction anisotropy suggesting that the hot tear shape (with or without IMCs) was mainly influenced by the morphology of the interdendritic channel network [24], which was contrived to be isotropic by the use of α-Al grain refiners.

The data shown so far describes the overall evolution of tears, however we also tracked the evolution of every individual hot tear with respect to time. We now present the evolution of the five largest final hot tears for each alloy and cooling rate combination because in engineering applications, it is the largest hot tears that are generally the most detrimental to mechanical performance. First we identified the five largest hot tears at the end of solidification, then these tears were tracked "backwards in time" to investigate how they formed directly and if they were the result of merging events. Fig. 11(a,b) plot the largest five hot tear areas for each experiment as a function of their number of merging events for Al-5Cu, without and with Fe respectively. For both alloys, the development of the largest hot tears always involved hot tear merging, sometimes with 30 or more merging events for a single large tear. Approximately, there was a linear relationship between the final size of the largest hot tears and the number of merging events. There was a steeper gradient for alloys containing IMCs because as shown in Figs. 3 and 9, hot tears tended to be more numerous and more regularly spaced, so merging was more likely. Hot tears in Al-5Cu could merge within a local cluster, but clusters tended not to merge with each other. This is the first time the dynamics of hot tear merging has been captured quantitatively, and suggests that the largest, most damaging hot tears are unlikely to arise from a single formation event, but evolve from a large number of hot tear merging events. These insights from relatively thin 2D samples, where biaxial rather than triaxial stress state likely predominate, should be confirmed by similar measurement obtained by tomography on 3D microstructures, assuming appropriate experimental conditions are available and can provide sufficient spatial and temporal resolution.

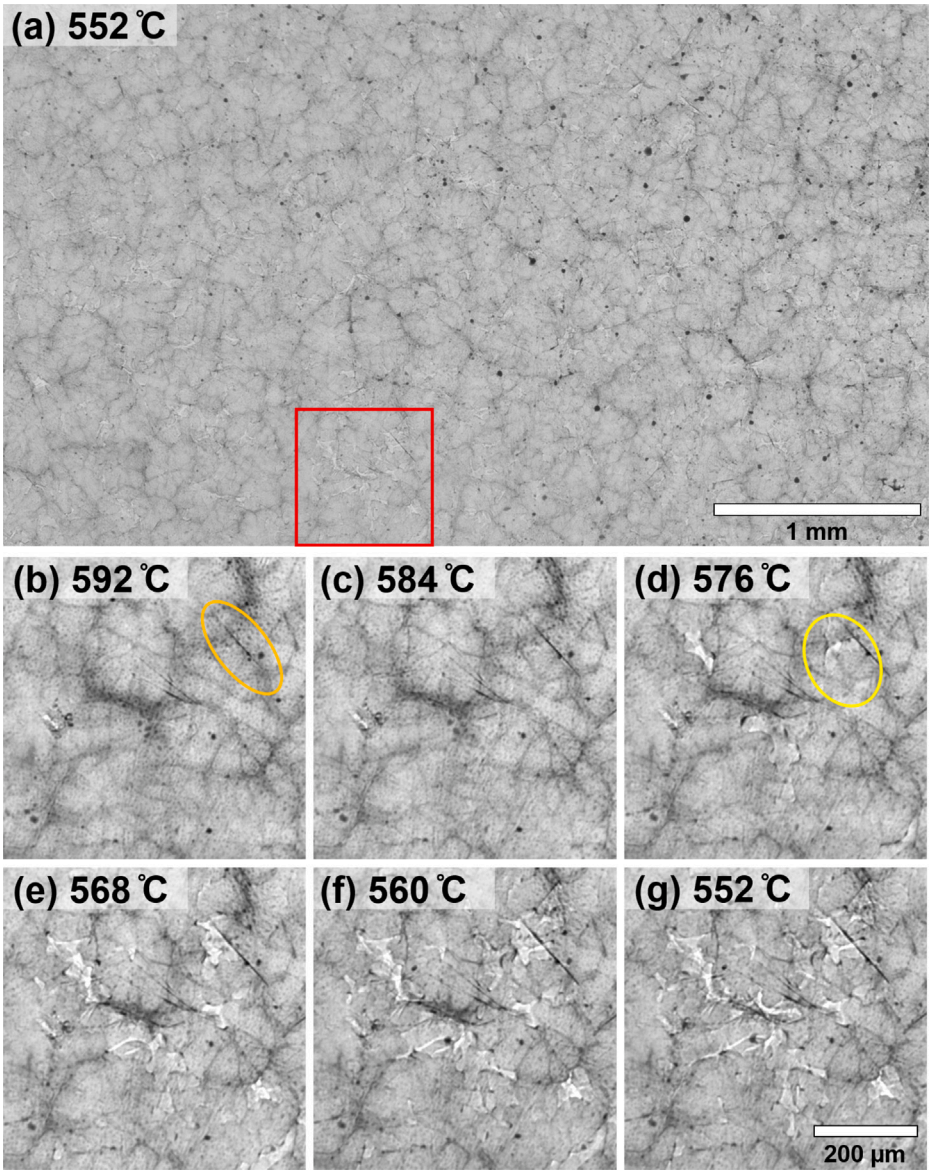

Fig. 5. Radiographic images showing the late stages of solidification of Al-5Cu-1Fe cooled at 0.5 °C s^{-1}. (a) Overall microstructure at 552 °C with the highlighted area in (a) shown in detail in (b–g) from 592 °C to 552 °C, corresponding to solid fractions between 0.83 and 0.89. The sequence shows the formation and growth of Al-Cu-Fe IMCs (orange circle) and hot tears (yellow circle). (For interpretation of the references to colour in this figure legend, the reader is referred to the web version of this article.)

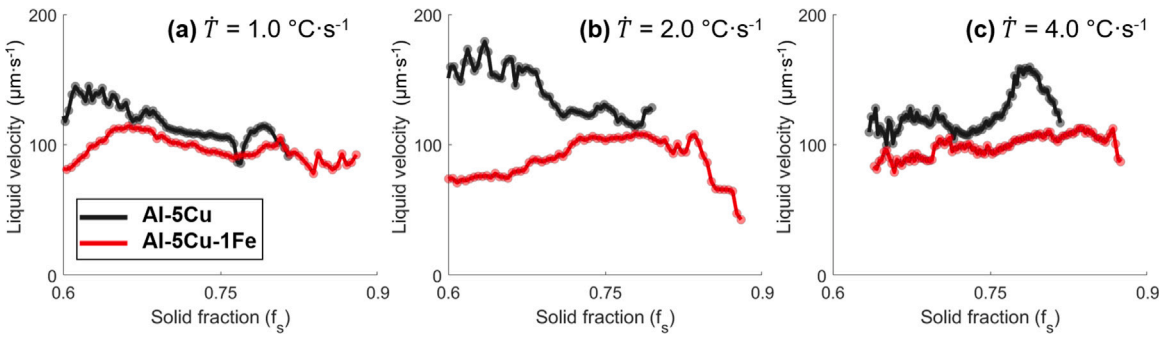

Fig. 6. Median velocity of the interdendritic liquid as a function of solid fraction at cooling rates of (a) 1.0 °C s^{-1}, (b) 2.0 °C s^{-1}, and (c) 4.0 °C s^{-1}. Each dataset was binned in solid fraction steps of 0.003. (For interpretation of the references to colour in this figure legend, the reader is referred to the web version of this article.)

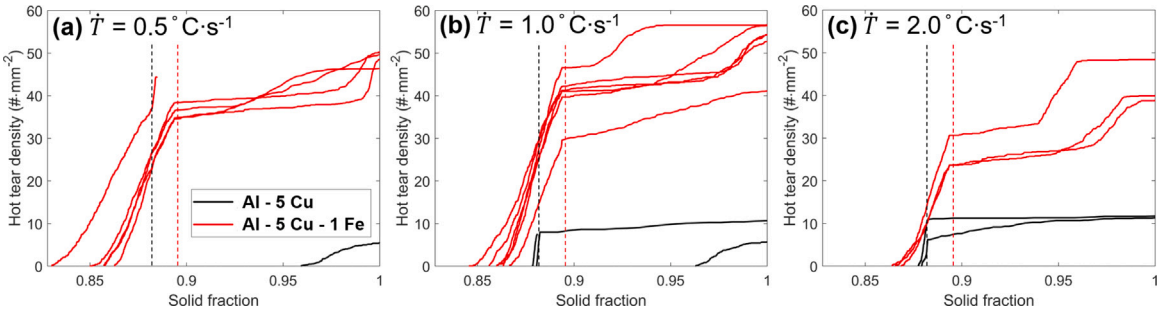

Fig. 7. Hot tear density as a function of solid fraction for Al-5Cu and Al-5Cu-1Fe at cooling rates of (a) 0.5 °C s^{-1} (b) 1.0 °C s^{-1} and (c) 2.0 °C s^{-1}. Each continuous line represents the data from one solidification sequence. The solid fractions at which the eutectic reaction starts are indicated by the vertical dashed lines at 0.882 and 0.896 respectively. (For interpretation of the references to colour in this figure legend, the reader is referred to the web version of this article.)

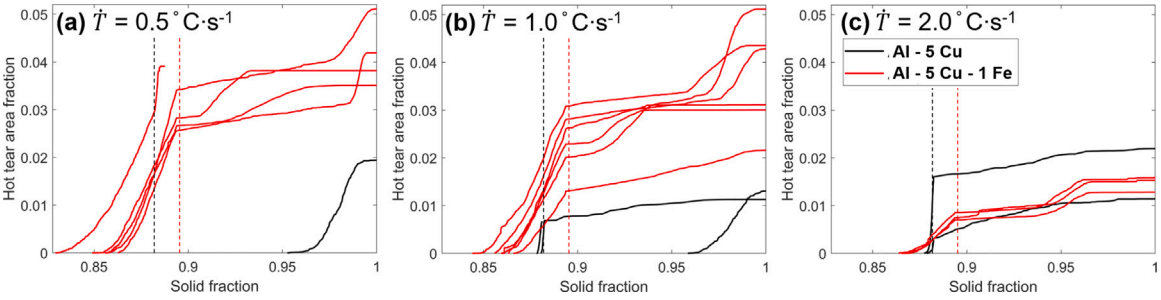

Fig. 8. Hot tear area fraction as a function of solid fraction for Al-5Cu (black curves) and Al-5Cu-1Fe (red curves) cooled at (a) 0.5 °C s^{-1}, (b) 1.0 °C s^{-1} and (c) 2.0 °C s^{-1}. Each continuous line represents the data from one solidification sequence. The solid fraction at the eutectic temperature are shown by the vertical dashed lines. (For interpretation of the references to colour in this figure legend, the reader is referred to the web version of this article.)

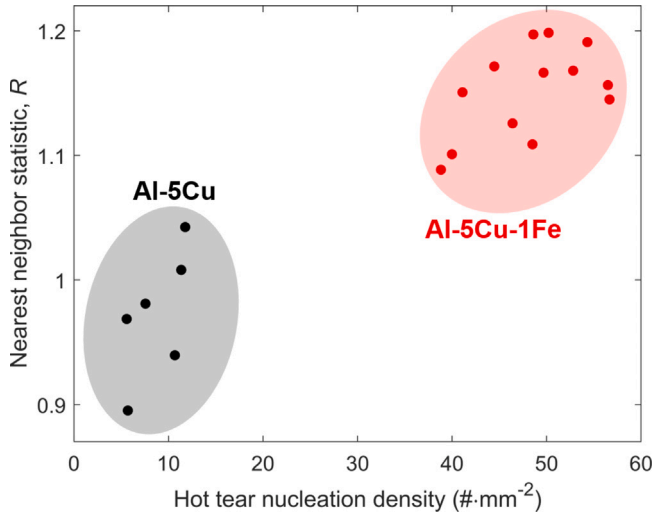

Fig. 9. The relationship between the randomness of hot tear spatial distribution R and the hot tear density for Al-5Cu and Al-5Cu-1Fe. (For interpretation of the references to colour in this figure legend, the reader is referred to the web version of this article.)

4. Conclusions

In situ X-ray radiography was used to investigate the formation and growth behaviour of hot tears in Al-5Cu and Al-5Cu-1Fe alloys during solidification. An automated hot tear detection, tracking and merging algorithm was developed and applied to probe the role of Fe-rich IMC particles on hot tear behaviour. A trace amount of Pb was added to the alloys to allow visualisation and quantification of late stage solidification interdendritic flow by tracking of micron-scale Pb droplets that formed through monotectic reaction. In comparison with Al-5Cu, hot tearing in Al-5Cu-1Fe was initiated at a lower solid fraction due to reduced interdendritic flow (feeding) resulting from the formation of IMCs that either partially or fully blocked the interdendritic channels, and reduced permeability. The presence of IMCs also made hot tear formation more spatially homogeneous and more numerous, so that merging of growing hot tears was more likely, which increased the overall final area fraction of hot tears. The largest hot tears were shown to arise from many hot tear merging events. In a flat temperature field with equiaxed primary α-Al grains, hot tears tended to grow in an approximately isotropic manner, whether large or small, and with or without IMCs.

The extent to which the insights on hot tearing in pseudo 2D geometries can be translated to 3D microstructures, more representative of cast alloys, should be explored by high speed 3D tomography. However, the availability of suitable hardware with comparable spatial and temporal resolution to radiography, sufficient thermal control, and availability of 3D tracking algorithms, remains a challenge. Nonetheless, the current work shows the growing possibilities for combining ever-more capable imaging and automated image analysis algorithms to move radiography and tomography from qualitative imaging to accurate quantification of key phenomena extracted from large datasets that ensure representative behaviour.

Declaration of competing interest

The authors declare that they have no known competing financial interests or personal relationships that could have appeared to influence the work reported in this paper.

Acknowledgements

We are grateful to Dr. Andrew Lui for assistance in the synchrotron-based radiography experiment and Ms. Ruining Jin for fruitful discussions. The work was supported by EPSRC, United Kingdom (UK) under grant number EP/N007638/1 (Future LiME Hub) and enabled by synchrotron beamtime (experiment No. I-20210153 EC) at the P05 beamline, operated by Helmholtz-Zentrum Hereon, at the DESY PETRA III synchrotron (Germany).

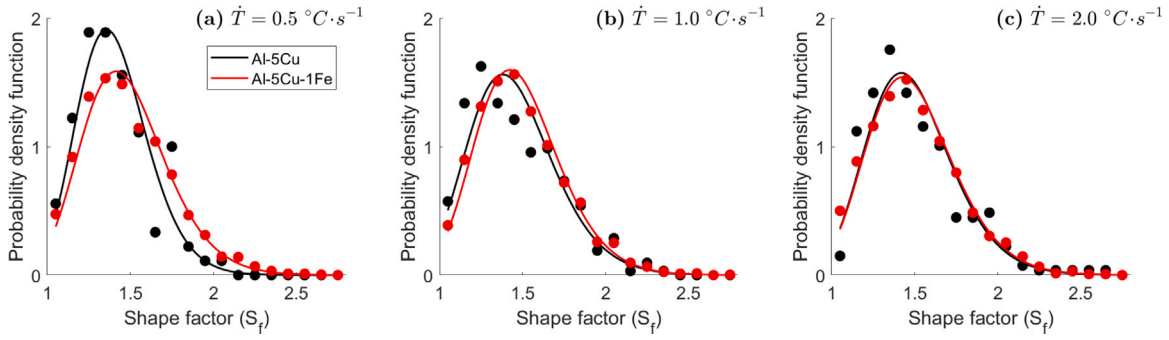

Fig. 10. Shape factor (S_f) distribution of fully-grown hot tears at cooling rates of (a) 0.5 °C s^{-1} (Al-5Cu: 90 cases and Al-5Cu-1Fe: 2788 cases) (b) 1.0 °C s^{-1} (Al-5Cu: 314 cases and Al-5Cu-1Fe: 3668 cases), and (c) 2.0 °C s^{-1} (Al-5Cu: 268 cases and Al-5Cu-1Fe: 1380 cases). The dataset is binned with a step size of 0.1 in S_f. (For interpretation of the references to colour in this figure legend, the reader is referred to the web version of this article.)

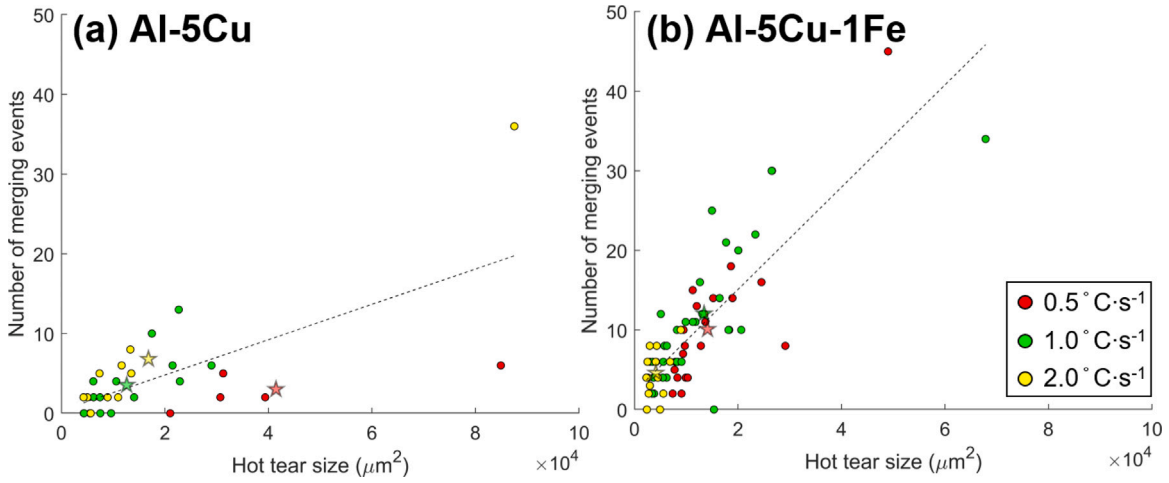

Fig. 11. The relationship between the number of merging events and the final size of the five largest hot tears for each solidification sequence for (a) Al-5Cu and (b) Al-5Cu-1Fe. The star symbols indicate the average size of hot tears and the average number of merging events for each experimental condition. The dashed lines are linear fit to all data points. (For interpretation of the references to colour in this figure legend, the reader is referred to the web version of this article.)

Appendix A. Supplementary data

Supplementary material related to this article can be found online at https://doi.org/10.1016/j.actamat.2023.119421.

References

[1] J. Campbell, Complete Casting Handbook: Metal Casting Processes, Metallurgy, Techniques and Design, Butterworth-Heinemann, 2015.
[2] M. Rappaz, J.-M. Drezet, M. Gremaud, A new hot-tearing criterion, Metall. Mater. Trans. A 30 (2) (1999) 449–455.
[3] M.A. Easton, H. Wang, J. Grandfield, C.J. Davidson, D.H. StJohn, L.D. Sweet, M.J. Couper, Observation and prediction of the hot tear susceptibility of ternary Al-Si-Mg alloys, Metall. Mater. Trans. A 43 (9) (2012) 3227–3238.
[4] M. Sistaninia, J.-M. Drezet, A.B. Phillion, M. Rappaz, Prediction of hot tear formation in vertical DC casting of aluminum billets using a granular approach, JOM 65 (9) (2013) 1131–1137.
[5] M. Sistaninia, S. Terzi, A.B. Phillion, J.-M. Drezet, M. Rappaz, 3-D granular modeling and in situ X-ray tomographic imaging: A comparative study of hot tearing formation and semi-solid deformation in Al–Cu alloys, Acta Mater. 61 (10) (2013) 3831–3841.
[6] C. Monroe, C. Beckermann, Prediction of hot tearing using a dimensionless Niyama criterion, JOM 66 (8) (2014) 1439–1445.
[7] C. Monroe, C. Beckermann, Development of a hot tear indicator for steel castings, Mater. Sci. Eng. A 413 (2005) 30–36.
[8] I. Farup, J.-M. Drezet, M. Rappaz, In situ observation of hot tearing formation in succinonitrile-acetone, Acta Mater. 49 (7) (2001) 1261–1269.
[9] S. Terzi, L. Salvo, M. Suéry, N. Limodin, J. Adrien, E. Maire, Y. Pannier, Mi. Bornert, D. Bernard, M. Felberbaum, et al., In situ X-ray tomography observation of inhomogeneous deformation in semi-solid aluminium alloys, Scr. Mater. 61 (5) (2009) 449–452.
[10] A.B. Phillion, R.W. Hamilton, D. Fuloria, A.C.L. Leung, P. Rockett, T. Connolley, P.D. Lee, In situ X-ray observation of semi-solid deformation and failure in Al–Cu alloys, Acta Mater. 59 (4) (2011) 1436–1444.
[11] J.W. Aveson, G. Reinhart, B. Billia, H. Nguyen-Thi, N. Mangelinck-Noël, T.A. Lafford, C.A. Vie, J. Baruchel, H.J. Stone, Observation of the initiation and propagation of solidification cracks by means of in situ synchrotron X-ray radiography, IOP Conf. Ser.: Mater. Sci. Eng. 33 (1) (2012) 012040.
[12] C. Puncreobutr, Peter D. Lee, R.W. Hamilton, B. Cai, T. Connolley, Synchrotron tomographic characterization of damage evolution during aluminum alloy solidification, Metall. Mater. Trans. A 44 (12) (2013) 5389–5395.
[13] C. Puncreobutr, A.B. Phillion, J.L. Fife, P.D. Lee, Coupling in situ synchrotron X-ray tomographic microscopy and numerical simulation to quantify the influence of intermetallic formation on permeability in aluminium–silicon–copper alloys, Acta Mater. 64 (2014) 316–325.
[14] H.K. Kamga, D. Larouche, M. Bournane, A. Rahem, Hot tearing of aluminum–copper B206 alloys with iron and silicon additions, Mater. Sci. Eng. A 527 (27–28) (2010) 7413–7423.
[15] L. Sweet, M.A. Easton, J.A. Taylor, J.F. Grandfield, C.J. Davidson, L. Lu, M.J. Couper, D.H. StJohn, Hot tear susceptibility of Al-Mg-Si-Fe alloys with varying iron contents, Metall. Mater. Trans. A 44 (12) (2013) 5396–5407.
[16] Suyitno, D.G. Eskin, L. Katgerman, Structure observations related to hot tearing of Al-Cu billets produced by direct-chill casting, Mater. Sci. Eng. A 420 (2006) 1–7.
[17] F. Liu, X. Zhu, S. Ji, Effects of Ni on the microstructure, hot tear and mechanical properties of Al–Zn–Mg–Cu alloys under as-cast condition, J. Alloys Compd. 821 (2020) 153458.
[18] T.W. Clyne, G.J. Davies, Comparison between experimental data and theoretical predictions relating to dependence of solidification cracking on composition, in: Solidification and Casting of Metals Proc. Conf., Sheffield, England, July 1977, 1979, pp. 275–278.
[19] M. Uludağ, R. Cetin, D. Dispinar, Freezing range, melt quality, and hot tearing in Al-Si alloys, Metall. Mater. Trans. A 49 (5) (2018) 1948–1961.

[20] E. Liotti, A. Lui, T. Connolley, P.S. Grant, Probing interdendritic flow and hot tearing during solidification using real time X-ray imaging and droplet tracking, Acta Mater. 240 (2022) 118298.
[21] M.R. Nasresfahani, M.J. Rajabloo, Research on the effect of pouring temperature on hot-tear susceptibility of A206 alloy by simulation, Metall. Mater. Trans. B 45 (5) (2014) 1827–1833.
[22] S. Li, K. Sadayappan, D. Apelian, Role of grain refinement in the hot tearing of cast Al-Cu alloy, Metall. Mater. Trans. B 44 (3) (2013) 614–623.
[23] J.A. Spittle, A.A. Cushway, Influences of superheat and grain structure on hot-tearing susceptibilities of AI-Cu alloy castings, Metals Technol. 10 (1) (1983) 6–13.
[24] Y. Yoshida, H. Esaka, K. Shinozuka, Effect of solidified structure on hot tear in Al-Cu alloy, IOP Conf. Ser.: Mater. Sci. Eng. 84 (1) (2015) 012059.
[25] P. Magnin, R. Trivedi, Eutectic growth: A modification of the Jackson and Hunt theory, Acta Metall. Mater. 39 (4) (1991) 453–467.
[26] E. Niyama, T. Uchida, M. Morikawa, S. Saito, Am. Foundrymen's soc, Int. Cast Met. J 7 (3) (1982) 52–63.
[27] M.E. Glicksman, R.J. Schaefer, J.D. Ayers, Dendritic growth-A test of theory, Metall. Trans. A 7 (11) (1976) 1747–1759.
[28] S.-C. Huang, M.E. Glicksman, Overview 12: Fundamentals of dendritic solidification—I. Steady-state tip growth, Acta Metall. 29 (5) (1981) 701–715.
[29] R. Trivedi, K. Somboonsuk, Constrained dendritic growth and spacing, Mater. Sci. Eng. 65 (1) (1984) 65–74.
[30] C. Puncreobutr, P.D. Lee, K.M. Kareh, T. Connolley, J.L. Fife, A.B. Phillion, Influence of Fe-rich intermetallics on solidification defects in Al–Si–Cu alloys, Acta Mater. 68 (2014) 42–51.
[31] R.S. Rana, R. Purohit, S. Das, Reviews on the influences of alloying elements on the microstructure and mechanical properties of aluminum alloys and aluminum alloy composites, Int. J. Sci. Res. Publ. 2 (6) (2012) 1–7.
[32] H. Yang, S. Ji, Z. Fan, Effect of heat treatment and fe content on the microstructure and mechanical properties of die-cast Al–Si–Cu alloys, Mater. Des. 85 (2015) 823–832.
[33] F. Wilde, M. Ogurreck, I. Greving, J.U. Hammel, F. Beckmann, A. Hipp, L. Lottermoser, I. Khokhriakov, P. Lytaev, T. Dose, et al., Micro-CT at the imaging beamline P05 at PETRA III, AIP Conf. Proc. 1741 (1) (2016) 030035.
[34] S. Feng, I. Han, A. Lui, R. Vincent, G. Ring, P.S. Grant, E. Liotti, Investigating metal solidification with X-ray imaging, Metals 12 (3) (2022) 395.
[35] I. Han, S. Feng, A. Lui, F. Wilde, P.S. Grant, E. Liotti, Tracking the evolution of hot tears in aluminium alloys using high-speed X-ray imaging, IOP Conf. Ser.: Mater. Sci. Eng. (2023).
[36] M. Dry, K. Preiss, J. Wagemans, Clustering, randomness and regularity: Spatial distributions and human performance on the traveling salesperson problem and minimum spanning tree problem, J. Probl. Solv. 4 (1) (2012) 1–17.
[37] C.W. Bale, E. Bélisle, P. Chartrand, S.A. Decterov, G. Eriksson, A.E. Gheribi, K. Hack, I.-H. Jung, Y.-B. Kang, J. Melançon, A.D. Pelton, S. Petersen, C. Robelin, J. Sangster, P. Spencer, M-A. Van Ende, FactSage thermochemical software and databases, 2010–2016, CALPHAD 54 (2016-09-01) 35–53, http://dx.doi.org/10.1016/j.calphad.2016.05.002.
[38] S. Feng, E. Liotti, A. Lui, S. Kumar, A. Mahadevegowda, K.A.Q. O'Reilly, P.S. Grant, An in-situ method to estimate the tip temperature and phase selection of secondary Fe-rich intermetallics using synchrotron X-ray radiography, Scr. Mater. 149 (2018) 44–48.
[39] C. Davidson, D. Viano, L. Lu, D. StJohn, Observation of crack initiation during hot tearing, Int. J. Cast Met. Res. 19 (1) (2006) 59–65.
[40] G. Cao, I. Haygood, S. Kou, Onset of hot tearing in ternary Mg-Al-Sr alloy castings, Metall. Mater. Trans. A 41 (2010) 2139–2150.
[41] S. Li, K. Sadayappan, D. Apelian, Characterisation of hot tearing in Al cast alloys: Methodology and procedures, Int. J. Cast Met. Res. 24 (2) (2011) 88–95.
[42] M. Sistaninia, A.B. Phillion, J.-M. Drezet, M. Rappaz, Three-dimensional granular model of semi-solid metallic alloys undergoing solidification: Fluid flow and localization of feeding, Acta Mater. 60 (9) (2012) 3902–3911.